Plume-ridge interactions: Ridge-ward versus plate-drag plume flow

Fengping Pang[1], Jie Liao[1,2,3], Maxim D. Ballmer[4], Lun Li[1,2,3]

[1]School of Earth Sciences and Engineering, Sun Yat-Sen University, Guangzhou 510275, China

[2]Guangdong Provincial Key Lab of Geodynamics and Geohazards, Guangzhou 510275, China

[3]Southern Marine Science and Engineering Guangdong Laboratory (Zhuhai), Zhuhai 519000, China

[4]Department of Earth Sciences, University College London, London, United Kingdom

Correspondence: Jie Liao (liaojie5@mail.sysu.edu.cn)

Abstract

The analysis of mid-ocean ridges and hotspots that are sourced by deep-rooted mantle plumes allows us to get a glimpse of mantle structure and dynamics. Dynamical interaction between ridge and plume processes have been widely proposed and studied, particularly in terms of ridge-ward plume flow. However, the effects of plate drag on plume-lithosphere and plume-ridge interaction remain poorly understood. In particular, the mechanisms that control plume flow towards vs. away from the ridge have not yet been systematically studied. Here, we use 2D thermomechanical numerical models of plume-ridge interaction to systematically explore the effects of (i) ridge spreading rate, (ii) initial plume head radius, and (iii) plume-ridge distance. Our numerical experiments suggest two different geodynamic regimes: (1) plume flow towards the ridge is favored by strong buoyant mantle plumes and small plume-ridge distances; (2) plume drag away from the ridge is in turn promoted by fast ridge

spreading, at least for small-to-intermediate plumes. We find that the pressure gradient between the buoyant plume and spreading ridge at first drives ridge-ward flow, but eventually the competition between plate drag and the gravitational force of plume flow along the base of the sloping lithosphere controls the fate of plume (spreading towards vs. away from the ridge). Our results highlight that fast-spreading ridges exert strong plate dragging force, which sheds new light on natural observations of largely absent plume-lithosphere interaction along fast-spreading ridges, such as the East Pacific Rise.

1 Introduction

Mid-ocean ridges (MORs) and hotspots are two main regions for deep material recycling to the surface of the Earth. However, these two units are not always isolated, but rather show strong interactions in some cases, termed as plume-ridge interaction (Morgan, 1978). Of up to 50 mantle plumes revealed by seismic tomography (French and Romanowicz, 2015; Montelli et al., 2004), more than 20 plumes are found to be associated with nearby ridges (Fig.1a; Ito et al., 2003). Plume-ridge interaction is manifested by geophysical and geochemical anomalies along the ridge axis, e.g., high mantle potential temperature (Dalton et al., 2014), enriched radiogenic isotope anomalies (Cushman et al., 2004; Douglass and Schilling, 1999; Yang et al. 2017), and adjacent lineations of seamounts (Ballmer et al., 2013b; Geissler et al., 2020; Lénat and Merle, 2009). Furthermore, plumes may promote migration of MOR spreading centers (Müller et al., 1998; Mittelstaedt et al., 2008, 2011; Whittaker et al., 2015), as evidenced by successive ridge jumps towards mantle plumes, e.g., at Iceland, Amsterdam-Saint Paul and Galapagos hotspots (Hardarson et al., 1997; Maia et al., 2011; Mittelstaedt et al., 2012). The interaction dynamics of a ridge with an on-axis and off-axis plume has been widely studied and modeled in analogue and numerical experiments, revealing that the major controlling factors involve the ridge spreading rate, plume buoyancy flux and their spatial distance (François et al., 2018; Ito et al., 1997; Kincaid et al., 1996; Ribe et al., 1995; Ribe, 1996; Sleep, 1997). Indeed, most plume-ridge interaction systems are associated with slow-spreading ridges and small mantle plumes and short plume-ridge distances (Fig.1b). However, numerical studies systematically investigating the effects of these parameters on plume-ridge interaction and quantify the controlling forces remain scarce.

As has been noted previously, buoyant plumes tend to spread ridge-ward along the sloping base of the lithosphere (Morgan, 1978; Schilling, 1991; Small, 1995). Regions of divergent mantle flow beneath MORs represent the lowest dynamic-pressure regions in the oceanic asthenosphere, and thus tend to suck ambient asthenospheric and plume materials towards the spreading center (Niu, 2014). On the other hand, the viscous drag at the base of the plate tends to convey the spreading plume material away from the MOR (Ribe and Christensen, 1994, 1999). Indeed, plume spreading at the base of the lithosphere is governed by the competition of trench-ward viscous plate drag vs. ridge-ward gravitational and pressure-driven forces (Kincaid et al.,1996). These gravitational and tectonic forces compete with other to control the regime of plume-ridge interaction, but their balance remains to be quantified.

The distribution of hotspots with classified as plume-ridge interaction (ridge-ward spreading) vs. no interaction (plate-drag spreading) also still remains enigmatic. Plume-ridge interaction is much more common near the Mid-Atlantic ridge (MAR) than near the East Pacific Rise (EPR) (Fig. 1a). Near the EPR, only the Pukapuka and Sojourn ridges display clear evidence of ridge-ward flow of the magmatic source, but these volcanic ridges have been attributed to a horizontally propagating viscous finger or small-scale convection, and not a mantle plume (Ballmer et al., 2013b; Clouard and Bonneville, 2005; Harmon et al., 2011). A previous study (Jellinek et al., 2003) proposed that fast-spreading ridges guide upwelling mantle flow towards the spreading center to convey the surrounding plumes from deep depth entirely into the MOR melting zone (Fig. 1c), resulting in the absence of hotspots adjacent to the EPR (see also Rowley et al., 2016; Rowley and Forte, 2022). However, fast plate spreading also tends to drag mantle plumes away from the MOR (Kincaid et al., 1995, 1996), leading to the typically parabolic shapes of hotspot swells such as near Hawaii (Ribe and Christensen,

1994). Whether the increased spreading rates in the Pacific vs. Atlantic promote ridge-ward vs. plate-drag plume flow remains an intriguing question.

The principal goal of this study is to investigate the process of plume-ridge interaction, with an emphasis on the effects of model parameters on the ridge-ward vs. plate-drag plume spreading. We explore the effects of various model parameters, such as the size of the plume, ridge spreading rate, and plume-ridge distance. Finally, we use our model results to interpret the difference of natural plume-ridge interaction systems in different oceans, particularly the striking difference between the East Pacific and Atlantic in this regard.
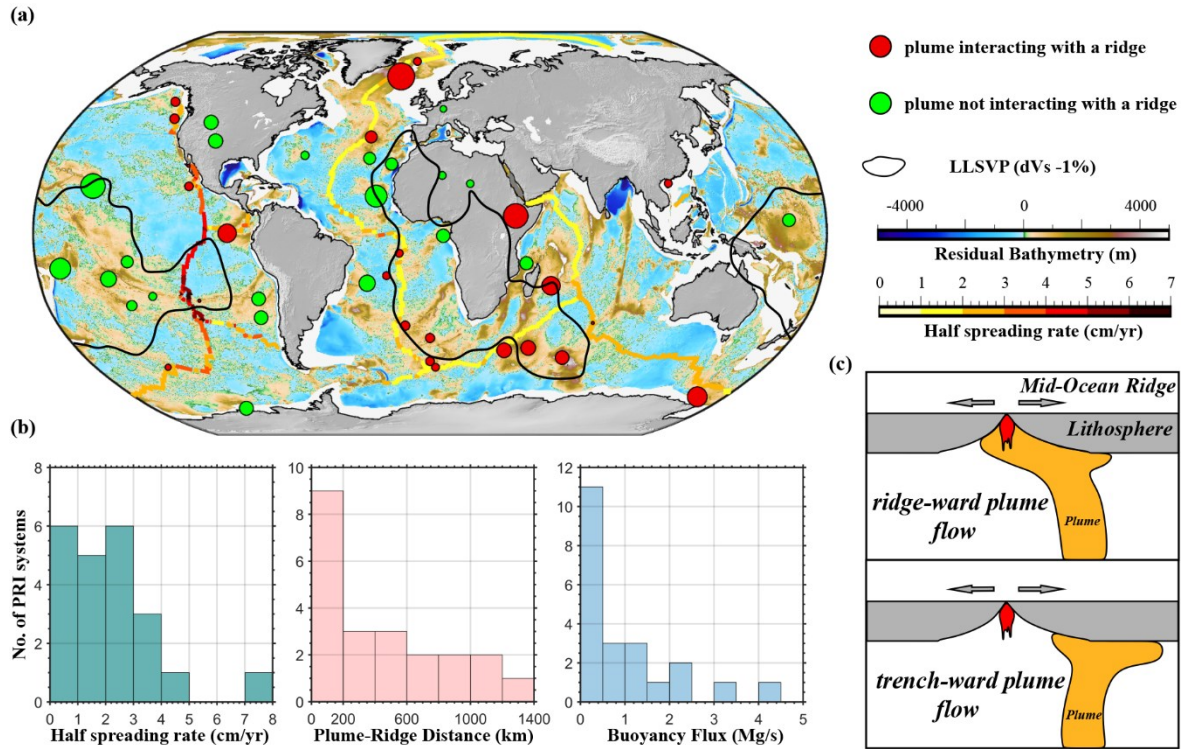
Figure 1. Global plume-ridge interaction systems. **(a)** Global distribution of mid-ocean ridges and mantle plumes. Residual bathymetry of the ocean basins come from Straume et al. (2019). Mid-ocean ridges are painted in color solid lines corresponding to half-spreading rate. Plumes not interacting with a ridge are shown by green circles, and hotspots linked to ridges are in red dots (Ito et al., 2003); size refers to the plume buoyancy flux from Hoggard (2020). Black lines denote the regions of two LLSVPs under the South Africa and Pacific Ocean (Torsvik et al., 2006). **(b)** Histograms of influential factors of plume-ridge interaction systems. Half spreading rate and plume-ridge distance is taken from GPlates (Müller et al., 2016; Whittaker et al., 2015). Plume-ridge interaction systems link to slow-spreading ridge and small mantle plumes and short plume-ridge distance. **(c)** Sketches of ridge-ward (top panel) and plate-drag plume flow (bottom panel) mode proposed, respectively.
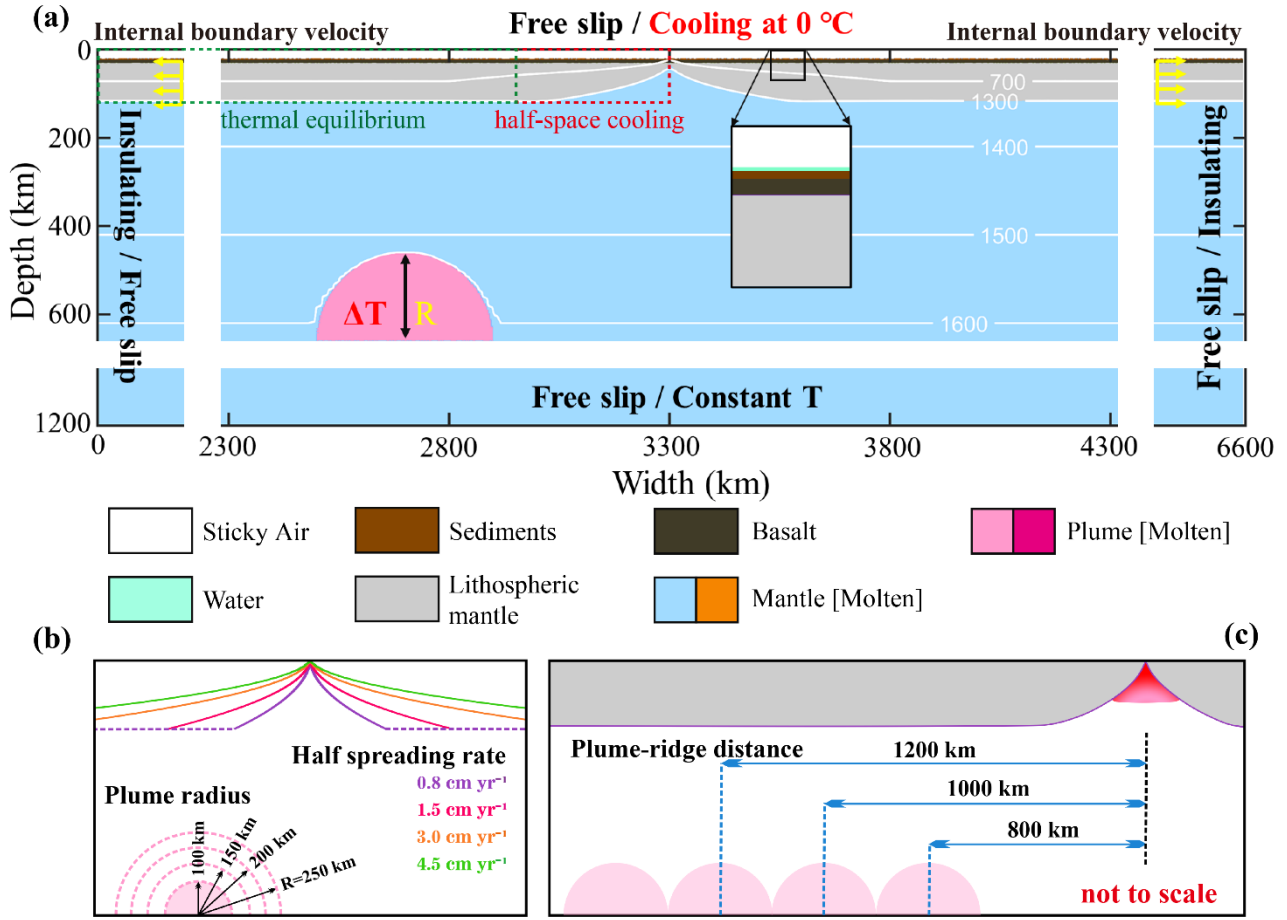
Figure 2. Model setup. **(a)** Initial composition and boundary conditions. The oceanic plate consists of half-space cooling part and the thermal equilibrium part. A 50-Myrs-old mid-ocean ridge sets in the middle of the model based on half-space cooling temperature structure. A thermal and chemical anormal mantle plume locates at 660 km. Different colors indicate the initial rock types and corresponding newly formed molten rock types. Yellow arrows are the half-spreading rates imposed internal in the lithosphere (i.e., from 20 km to 120 km in depth) to simulate ridge spreading. **(b)** Initial tested ridge and plume configurations. **(c)** Initial tested plume-ridge distances.

2   Numerical modelling

2.1 Modelling methods

To explore plume-lithosphere and plume-ridge interaction, we conduct numerical simulations

7

104   utilizing the 2D thermo-mechanical code I2VIS, which is based on staggered finite difference method

105   combined with marker-in-cell techniques (Gerya and Yuen, 2003, 2007). This modeling framework

106   uses both Eulerian grids and randomly-distributed Lagrangian markers to jointly solve equations of

107   conservation of mass, momentum and energy (Eq. (1)-(3), respectively):

108    $$\nabla \cdot \vec{v} = 0 \quad (1)$$

109    $$\frac{\partial \sigma'_{ij}}{\partial x_j} - \frac{\partial P}{\partial x_i} + \rho g_i = 0 \quad (2)$$

110    $$\rho C_p \left(\frac{DT}{Dt} \right) = -\nabla \cdot \vec{q} + H_r + H_a + H_s + H_l \quad (3)$$

111   where v refers to the velocity, σ'_{ij} the deviatoric stress tensor, P the pressure, ρ the density, g the

112   gravity acceleration, $\frac{D}{Dt}$ the Lagrangian time derivative, C_p the heat capacity, and q the heat flux.

113   Additionally, H_r, H_a, H_s, and H_l are the radioactive, adiabatic, shear, and latent heat productions,

114   respectively.

115   We employ a non-Newtonian visco-plastic rheology (Gerya and Yuen, 2007) in the models. The

116   viscous rheology depends on stress, temperature and pressure. The appropriate viscosity is expressed

117   as that of a composite diffusion and dislocation-creep material (Eq. (4)).

118    $$\frac{1}{\eta_{vis}} = \frac{1}{\eta_{diff}} + \frac{1}{\eta_{disl}} \quad (4)$$

119   in which η_{diff} and η_{disl} are the diffusion and dislocation creep viscosity, respectively, and can be

120   further computed as Eq. (5) and Eq. (6):

121    $$\eta_{diff} = \frac{1}{2} A \sigma_{crit}^{1-n} \exp \left(\frac{PV_a + E_a}{RT} \right) \quad (5)$$

122    $$\eta_{disl} = \frac{1}{2} A^{\frac{1}{n}} \dot{\varepsilon}_{II}^{\frac{1-n}{n}} \exp \left(\frac{PV_a + E_a}{nRT} \right) \quad (6)$$

123   where P is the pressure, T is the temperature, $\dot{\varepsilon}_{II}$ is the second invariant of the strain rate tensor, σ_{crit}

124   is the diffusion-dislocation creep transition stress, and A, E_a, V_a, and n are the strain rate pre-

125   exponential factor, activation energy, activation volume, and stress exponent, respectively. The plastic

126   behavior η_{pla} is described by the Drucker-Prager yield criterion (Byerlee, 1978; Ranalli, 1995)

127   according to Eq. (7) and Eq. (8):

128    $$\sigma_y = C + P\varphi \quad (7)$$

129    $$\eta_{pla} = \frac{\sigma_y}{2\dot{\varepsilon}_{II}} \quad (8)$$

130   in which σ_y is the yield stress, C is the rock cohesion and φ is the effective friction coefficient. The

131   effective viscosity η_{eff} of rocks is thus constrained by both viscous and plastic deformation, where

132   the rheological behavior depends on the minimum viscosity attained between ductile and brittle fields:

133    $$\eta_{eff} = \min(\eta_{vis}, \eta_{pla}) \quad (9)$$

134   Partial melting, melt extraction and percolation are also considered in the model in a simplified

135   way (Gerya, 2013). The melt fraction (M_0) of the crust are assumed to increase with temperature and

136   are calculated according to Eq. (10):

137    $$M_0 = 0 \text{ when } T \leq T_{solidus}$$

138    $$M_0 = \frac{(T - T_{solidus})}{(T_{liquidus} - T_{solidus})} \text{ when } T_{solidus} < T < T_{liquidus} \quad (10)$$

139    $$M_0 = 1 \text{ when } T \geq T_{liquidus}$$

140   where $T_{solidus}$ and $T_{liquidus}$ are the solidus and liquidus temperature of different rock types,

141   respectively, taken from Katz et al. (2003).

142   In our model, melt extraction is modeled indirectly and considered as an instantaneous process

143   (Gerya et al., 2015). The extracted melt is assumed to move vertically from the molten source and then

144   added to the bottom of the crust. Partial melt is extracted from the mantle and instantaneously displaced

145   to the bottom of the crust and converted into hot mafic magma, obeying the conservation of material.

146   The amount of extracted melt during the evolution of each experiment is traced by the Lagrangian

147   markers (Gerya, 2013). The total amount of melt, M, for every marker excludes the amount of

148 previously extracted melt according to Eq. (11):

$$M = M_0 - \Sigma_n M_{ext} \quad (11)$$

150 where $\Sigma_n M_{ext}$ refers to the total melt fraction extracted during the previous n melt extraction

151 timesteps.

152   The effective density of mafic magma and molten crust depends on its melt fraction and is

153 calculated as (Gerya et al., 2015; Gülcher et al., 2020):

$$\rho_{eff} = \rho_{solid}(1 - M + M \frac{\rho_{0,molten}}{\rho_{0,solid}}) \quad (12)$$

155 where $\rho_{0,molten}$ and $\rho_{0,solid}$ are the reference densities of the molten and solid crust. ρ_{solid} is the

156 crust density at given pressure and temperature, which can be computed as:

$$\rho_{solid} = \rho_{0,solid}[1 - \alpha(T - 298)][1 + \beta(P - 0.1)] \quad (13)$$

158 with thermal expansion $\alpha = 3 \times 10^{-5} K^{-1}$ and compressibility $\beta = 10^{-11} Pa^{-1}$.

159   Surface processes, such as erosion and sedimentation, are considered by solving the transport

160 equation on the Eulerian nodes at each time step (Gerya and Yuen, 2003). Our erosion/sedimentation

161 model uses gross-scale erosion/sedimentation rates which are independent of local elevation and

162 topography (Burov and Cloetingh, 1997). We use constant and moderate rates of erosion (0.315 mm/yr)

163 and sedimentation (0.0315 mm/yr), respectively, which falls within naturally observed ranges.

164

165 **2.2 Model setup**

166   The size of the model box is 6600 × 1200 km, with a nonuniform grid of 501 × 301

167 computational nodes in length and depth, respectively (Fig. 2). The densest grid is located in the center

168 of the model domain (i.e., grid size decreases linearly from 20 km at the edges to 2 km at the ridge

169 axis), where plume-ridge interaction would happen. The model consists of a 20 km thick sticky air

layer to accommodate crustal surface deformation. To reproduce the oceanic lithosphere, we choose a

typical layered model, where the crust is composed of a water level (2 km), a sediment layer (1.5 km),

and a basalt layer (7.5 km). The oceanic lithosphere and asthenosphere in the model are both modeled

as dry olivine (the different colors for the mantle lithosphere and asthenosphere in the figures of this

paper are only for better visualization). Besides, a 50-Myrs-old mid-ocean ridge is set on central part

of the lithosphere, splitting the model domain into two parts. At the depth of 660 km, a 200-km-wide

semicircular plume is located on the left of model domain, corresponding to the onset of plume-ridge

interaction from the mantle transition zone. Detailed rock parameters are listed in Table 1.

The thermal conditions at the top and bottom boundaries are fixed at 273 and 2513 K, respectively.

The left and right boundaries are both insulating, with no external heat flow across them. The initial

temperature structure of the mantle is adiabatic (0.5 K km^{-1}), which results in a temperature at 660 km

depth of 1843 K. The initial temperature structure of the oceanic plate consists of half-space cooling

part and thermal equilibrium part (Fig. 2a). The half-space cooling model is used to describe the

oceanic plate younger than 50 Myr, and the thermal equilibrium structure is used to describe older

oceanic parts. In other words, the thermal age of the lithosphere far away from the ridge is fixed at 50

Myr with a constant plate thickness (i.e., ~100 km). The hot plume is set a circular thermal and

compositional (see Table 1) anomaly with an excess temperature of 250 K to trigger a rising

thermochemical plume. All the velocity boundaries are free slip boundaries. Additional internal

boundary velocities are imposed at 500 km from each side boundary in the lithosphere to maintain the

imposed half spreading rate (Fig. 2a).

Table 1. Rock physical properties used in the numerical models.

Parameters	Sediments	Ocean Crust	Mantle	Plume	Reference [a]
Flow law	Wet quartz	Basalt	Dry olivine	Wet olivine	
Preexponential factor $A(Pa^n s)$	1.97×10^{17}	4.80×10^{22}	3.98×10^{16}	5.01×10^{20}	1
Activation energy E_a(KJ mol^{-1})	154	238	532	470	1
Activation volume V_a(J bar^{-1}mol^{-1})	0	0	1	0.8	1
Exponent n	2.3	3.2	3.5	4	1
Cohesion C(Pa)	2×10^7	2×10^7	2×10^7	2×10^7	1
Effective friction coefficient φ	0.6/0.3	0.6/0.3	0.6/0.3	0.6/0.3	1
Density ρ(Kg m^{-3})	2600	3000	3300	3270	2
Radioactive heating H_r(W m^{-3})	2×10^{-6}	2.2×10^{-7}	2.2×10^{-8}	2.5×10^{-8}	2

192　a: 1-(Ranalli, 1995), 2-(Turcotte and Schubert, 2014)

193　Other physical parameters used for all rocks include: gas constant R=8.314 J K^{-1}mol^{-1}, thermal

194　expansion α=3×10^{-5}K^{-1}, compressibility β=1×10^{-11} Pa^{-1}, heat capacity Cp=1000 J kg^{-1}K^{-1}.

195

196　## 3　Model Results

197　　　We conduct a series of numerical experiments to investigate ridge suction versus plate drag acts

198　on plumes. The effects of three major model parameters (i.e., the spreading rate of mid-ocean ridge,

199　the initial plume head radius, and the plume-ridge distance) are systematiclly studied. The typical

200　dynamic evolution of models with ridge-ward vs. plate-drag plume flow are demonstrated.

201　### 3.1 Model evolution with ridge-ward plume flow

202　　　For models with dominant ridge-ward flow, the typical model evolution is shown in Fig. 3 (the

203　major model parameters used in this case are: the half spreading rate of 8 mm yr^{-1}, the initial plume

204　head radius of 200 km, and the off-axis distance of 800 km). In the early plume head stage, the buoyant

205　mantle plume rises up rapidly in a mushroom-like shape (Fig. 3b) and imposes dynamic stresses at the

206　base of the overriding oceanic plate, leading to significant surface uplift (Fig. 3a). The ascending plume

experiences extensive decompression melting at the base of the overriding plate, and due to the dynamic overpressure, spreads laterally, forming two branches that flow in opposite directions (Fig. 3c). A large amount of plume material is eventually entrained towards the spreading center, ponding underneath the ridge axis, and significantly affecting the ridge dynamics. The entrainment of hot plume material promotes decompression melting (Figs. 3d, e) and increases the temperature beneath the ridge (Fig. S2). Within the overlying lithosphere, the buoyant mantle plume leads to stress localization and strongly weakens the oceanic plate (Figs. S1, S3). As the plume eventually flows upward along the increasingly sloping base of the plate near the MOR, massive melting and crust production occurs (Fig. S1), forming an oceanic plateau of thickened crust. In addition to this gravitational force that guides plume material of the right branch ridge-ward, plate spreading drags both branches in the opposite direction. Moreover, convective and tectonic stresses ("plume push" and "ridge suction") affect both branches of the plume in a different way. As a consequence, the two branches evolve asymmetrically: the right branch that flows towards the ridge axis is more vigorous than the left branch, and the plume tail is also tilted towards the spreading center (Figs. 3c-e). For a more detailed discussion of the underling controlling forces, see below.
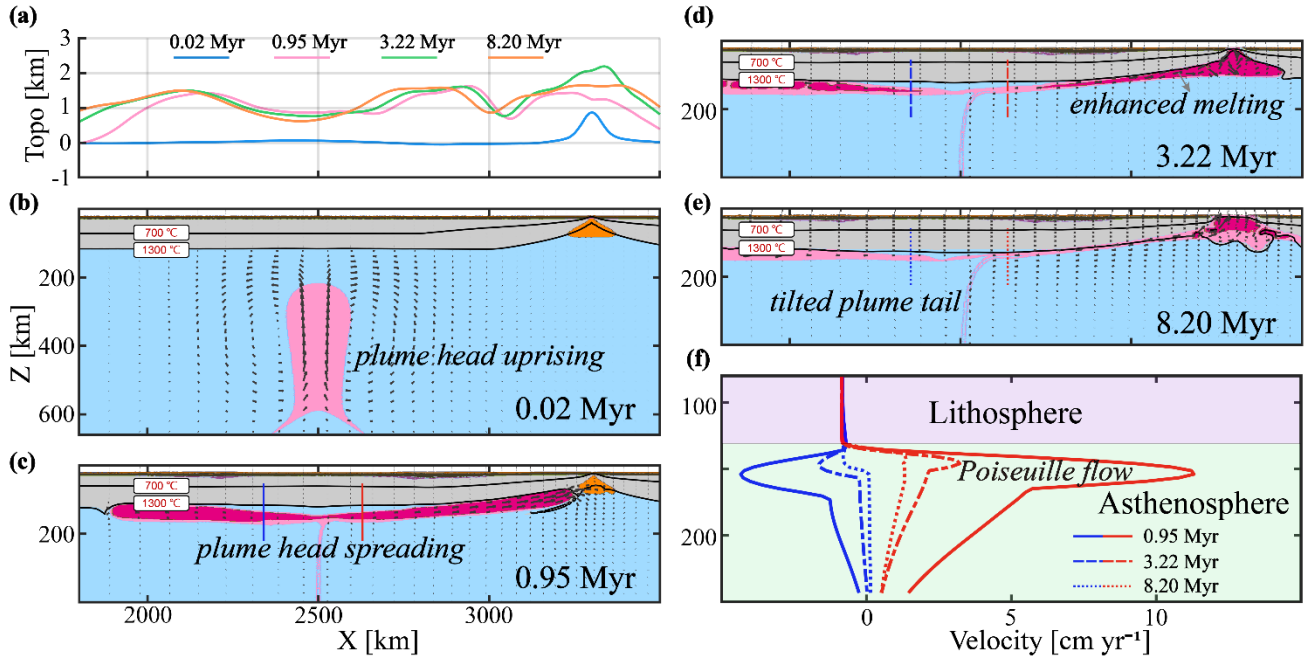
Figure 3. The evolution of the reference model M12 (see Table S1 in supplementary material) with dominant ridge-ward plume flow. The main model parameters employed in this case are: half spreading rate of 8 mm yr^{-1}, an initial plume head radius of 200 km, and an off-axis distance of 800 km. **(a)** surface topography over time along the flow path. **(b-e)** Snapshots of composition for the reference model (M12). **(f)** Profiles of the horizontal velocity component over time at the sections as indicated (color-coded) in panel (c-e).

The mantle flow horizontal velocity profiles (Fig. 3f) further demonstrate the dominance of ridge-ward plume flow, showing that plume flow is faster towards the spreading ridge than away from it. The velocity profiles elucidate dominant Poiseuille flow, with the maximum flow velocities in the middle of the asthenospheric channel. Such velocity profiles are well consistent with observations of seismic anisotropy at the Reunion plume (Barruol et al. 2019). The branches of the spreading plume head move significantly faster than the overriding plate. Therefore, plate drag actually slows down the spreading of the plume branches in this model case. Because of the asymmetrical spreading of the

14

238 plume head, the buoyancy flux carried by the right branch of the plume (density anomaly multiplied

239 by horizontal velocity from Figure 3f) is also much larger than that carried by the left branch.

240

3.2 Model evolution with plate-drag plume flow

242   For models with dominant plume flow away from the ridge ("plate-drag flow"), the typical model

243 evolution is shown in Fig. 4. The controlling parameters of the representative model shown in Figure

244 4 are the same as for the model shown in Figure 3, except for a smaller radius (100 km) and faster

245 spreading ridge (half spreading rate: 45 mm yr^{-1}). At first, the ascending plume head spreads out

246 similarly as in the case described above and interacts with the overriding oceanic lithosphere. The

247 largest surface uplift is sustained just above the plume head (Fig. 4a), slightly different from the

248 previous model in which the highest surface elevation is observed on both sides of the plume conduit

249 (Fig. 3a). Related to this spreading and uplift, divergent stresses are sustained in the overlying

250 lithosphere (Fig. S4), but no weakening or yielding occurs (Fig. S6). The plume head undergoes

251 significant decompression melting near the deflection point (Fig. 4c). However, thick and cold

252 lithosphere prevents magma from extracting (Fig. S4). As the plume cools, partially molten plume gets

253 solidified speedily (Figs. 4d-e and S5). In contrast to the reference model from section 3.1, this model

254 displays most plume material flowing away from the ridge, likely due to dominant plate drag (Figs.

255 4c-e). Indeed, the left branch of the plume consistently displays larger buoyancy fluxes and maximum

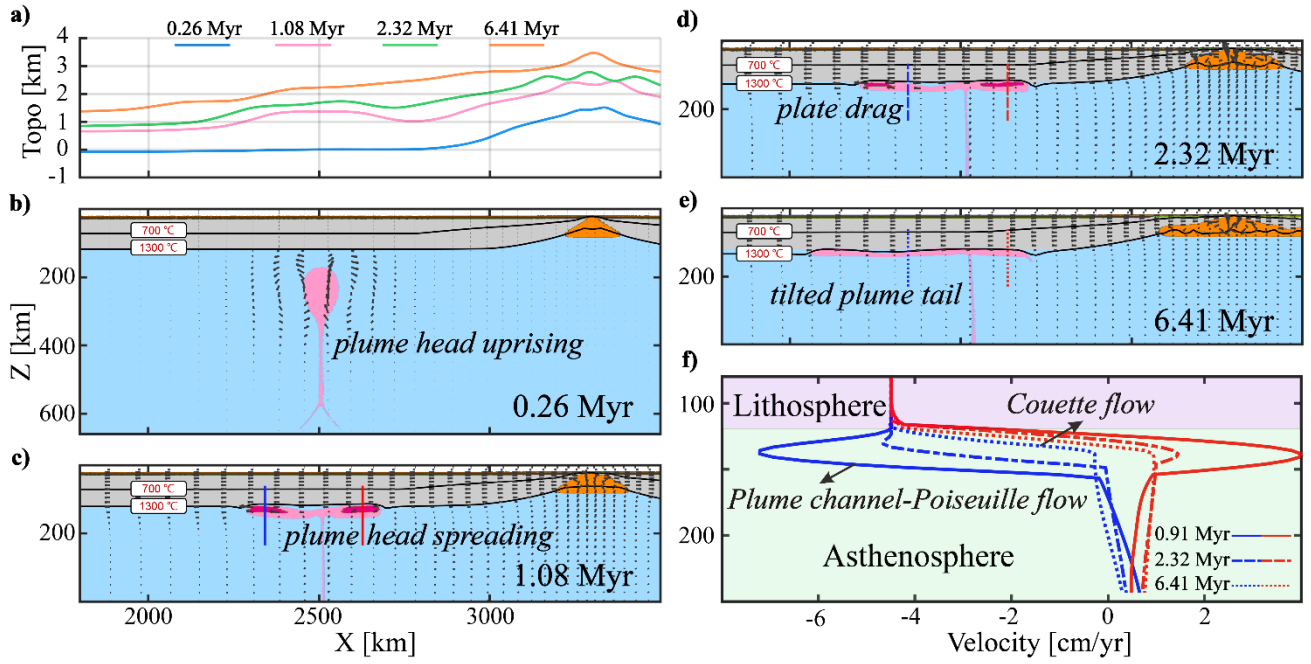256 velocities than the right side over time (Fig. 4f).

257

Figure 4. Same as Figure 3 for case M77 (i.e., the reference model for the plate-drag plume flow regime). The main model parameters employed in this case are: half spreading rate of 45 mm yr^{-1}, an initial plume head radius of 100 km, and an off-axis distance of 800 km.

The underlying mechanism for dominant plate-drag plume flow is the frictional shear force of the moving plate, which is further demonstrated by the plume flow velocity profiles (Fig. 4f). In the early plume head stage (~1.08 Myr), the plume spreads out faster than plate velocity, which is primarily driven by the overpressure of the ponding plume head at this stage. After a short amount of time (~2.32 Myr), however, plume spreading becomes significantly slower than plate velocity, and hence plate drag drives and controls the plume flow. Indeed, the flow mode in the asthenosphere rapidly shifts from Poiseuille flow (i.e., active plume flow) to Couette flow (i.e., passive plume flow) (Fig. 4f), indicating the increasing role of plate drag on plume flow, soon after an initial of plume-head spreading.
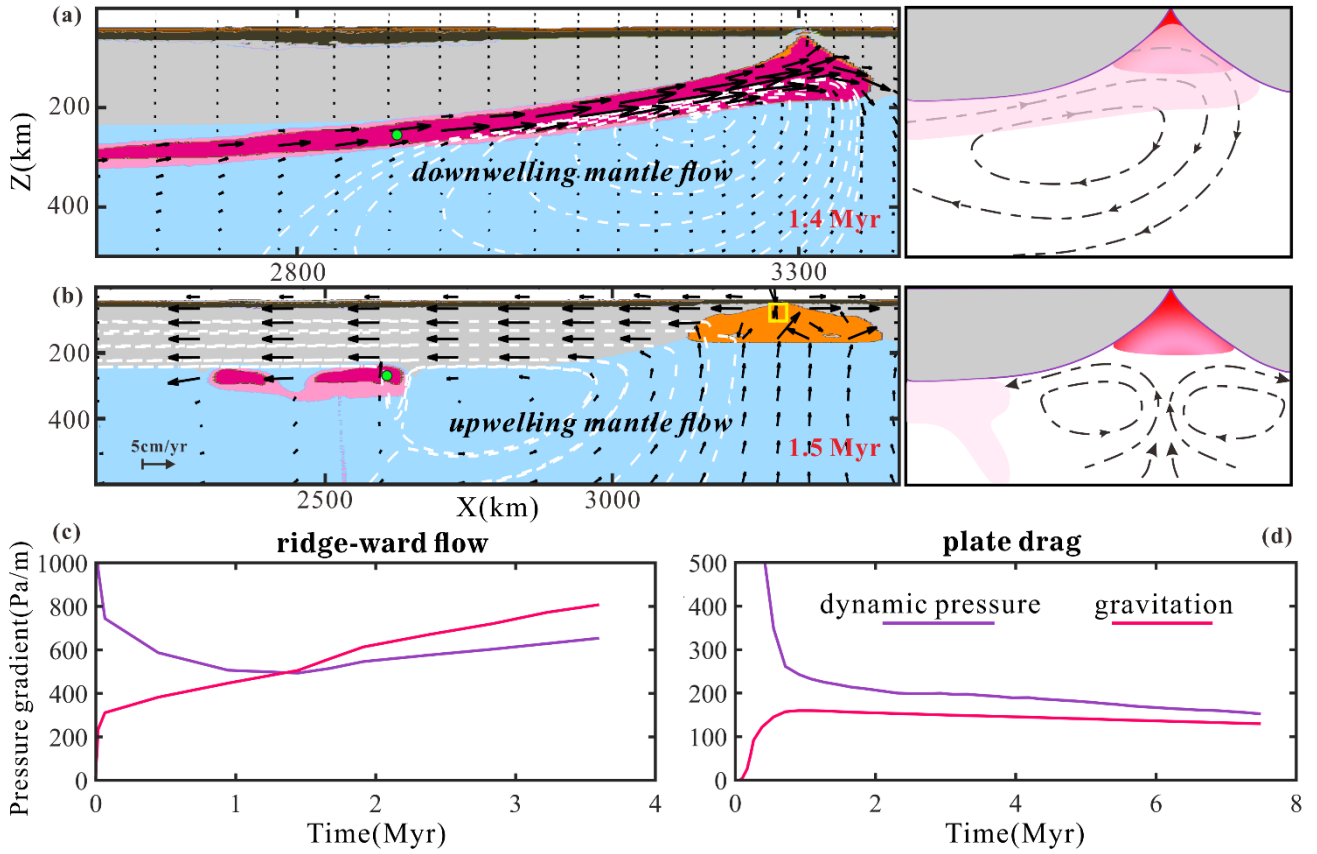
Figure 5. Comparsion between models with ridge-ward vs. plate-drag plume flow. **(a)** Ridge-ward flow with downwelling beneath the MOR (results from case M12 as in Figure 3). White dashed lines are streamlines; black arrows visualize the flow field. Schematic of flow in the sub-panel on the right-hand side. **(b)** Plate-drag flow with upwelling mantle corner flow beneath the MOR (results from case M77 as in Figure 4). **(c)** The dynamic pressure and gravitational gradient of plume marker (i.e. green circle in (a)) over time. The yellow box in (b) marks the location for the computation of average dynamic pressure at the ridge, needed for the calculation of the dynamic pressure gradient (see text). **(d)** The dynamic pressure and gravitational gradient of plume marker (i.e. green circle in (b)) over time.

3.3 Two modes of plume-lithosphere interaction

284   The dominant ridge-ward and dominant plate-drag plume flow regimes are two distinct modes of

285 plume-plate interaction. The differences between these two regimes are further demonstrated in

286 terms of mantle flow (Figs. 5a,b), driving forces (Figs. 5c,d).

287   In the ridge-ward dominated models, clockwise mantle develops from the plume to the spreading

288 ridge (Fig. 5a). A large amount of molten plume material flows to the spreading ridge and occupies

289 the space underneath the ridge axis, sustaining significant asymmetry of mid-ocean ridge melting

290 (Conder et al., 2002). As a consequence to the continuous supply of the plume material, downward

291 mantle flow forms beneath the ridge axis. This flow pattern dramatically differs from that shown in

292 the plate-drag dominated models, which show upward mantle flow underneath the ridge axis (Fig.

293 5b), as typical for the flow beneath a MOR without the influence of a plume.

294   The distinct modes of plume-ridge interaction (ridge-ward vs. plate-drag flow) are controlled by

295 the competition of the tectonic (plate drag, ridge suction) and gravitational (plume buoyancy) driving

296 forces. On one hand, The moving plate drags sub-lithospheric plume material away from the ridge. On

297 the other hand, the mechanism of ridge-ward flow is twofold. First, the buoyant plume material flows

298 along the sloping base of the lithosphere towards the shallow ridge along the gravitational gradient.

299 Second, the plume is driven along the dynamic-pressure gradient from the pressure maximum (e.g.,

300 where the plume sustains dynamic topograph) towards the pressure minumum beneath the diverging

301 ridge. These gravitational (G_{gv}) and pressure-driven (G_{dp}) gradients are calculated by tracing plume

302 markers (Figs. 5c,d) as follows:

$$G_{dp} = (P_{mk} - P_r)/L \qquad (12)$$

$$G_{gv} = (\rho_0 - \rho_{mk}) * g * k \qquad (13)$$

305 where P_{mk} is the dynamic pressure of plume marker and P_r is the averaged pressure in a 50 km box

306 at ridge center (Fig. 5b); L is the horizontal distance from plume marker to ridge axis; ρ_{mk} and ρ_0

307 are the plume marker density and initial density, respectively; g is the gravitational acceleration; k is

308 the local slope of the base of the lithosphere.

309   In the early stage of model evolution, the plume head's dynamic overpressure is dominant, driving

310 plume spreading in both directions (Fig. 5c), in particular in the direction of the low-pressure ridge.

311 However, this pressure gradient systematically diminishes over time as the plume (head) spreads. Once

312 the spreading plume approaches the ridge, the lithospheric slope increases. At some point, the

313 gravitational gradient exceeds the dynamic pressure gradient, taking over as the major driving force of

314 guiding plume material towards the ridge. Consequently, one of the essential conditions for plume-

315 ridge interaction is that the plume must be able to reach the critical zone near the ridge, where the slope

316 is sufficiently steep to take over for the ever diminishing pressure gradient. This implies that the plume

317 buoyancy must (1) overcome the shearing force of plate drag, and (2) the pressure-gradient must be

318 sustained long enough to reach the critical zone, in which the gravitational gradient can take over. The

319 (1) shearing force scales with the rate of ridge spreading, and the (2) critical zone is more readily

320 reached for high buoyancy fluxes at a given plume-ridge distance.

321

322

323 **3.4 Influence of model parameters**

324   We have systematically investigated the effect of the three main model parameters (i.e., the

325 spreading rate of the mid-ocean ridge, initial plume head radius and plume-ridge distance) on plume-

326 ridge interaction. We explored half spreading rates of the ridge of 8, 15, 30, and 45 mm yr^{-1},

corresponding to ultra-slow, slow, medium, and fast-spreading mid-ocean ridges, respectively (Gerya, 2012). We varied initial plume head radii in the range of 100 km to 300 km. Further, we tested plume-ridge distance in the range of 600 to 1400 km.

3.4.1 Plume head radius

The size of the buoyant plume exerts an important control on plume-ridge interaction. Small plumes tend to be dragged away from the ridge, with typically larger lateral fluxes of the left branch than the right branch of the spreading plume (Figs. 6a,b). The buoyancy flux in each branch is calculated by multiplying the velocity of the markers in plume pipe (Figs. 6d-f) by the density. The dynamic pressure decreases with decreasing plume size (Fig. S8a), and the pressures gradient is thus not strong enough for small plumes to reach the ridge. Plate shearing dominates plume flow soon after plume head spreading, and the moving plate then drags plume head material, leaving a tilted plume tail (Fig. 6d). In contrast, with larger initial plume head radius or buoyancy flux, the ponding plume spreads more vigorously (Fig. 6c) and sustains much higher overpressures at the base of the plate (Fig. S8a). This vigorous spreading can overcome plate drag to drive Poiseuille flow in both directions. Once the right plume branch approaches the spreading center, it is attracted and further accelerated by ridge suction. The plume tail is also markedly tilted towards the ridge axis due to asymmetric spreading (Fig. 6f). The larger the plume is, the more plume material gets entrained by the spreading center.
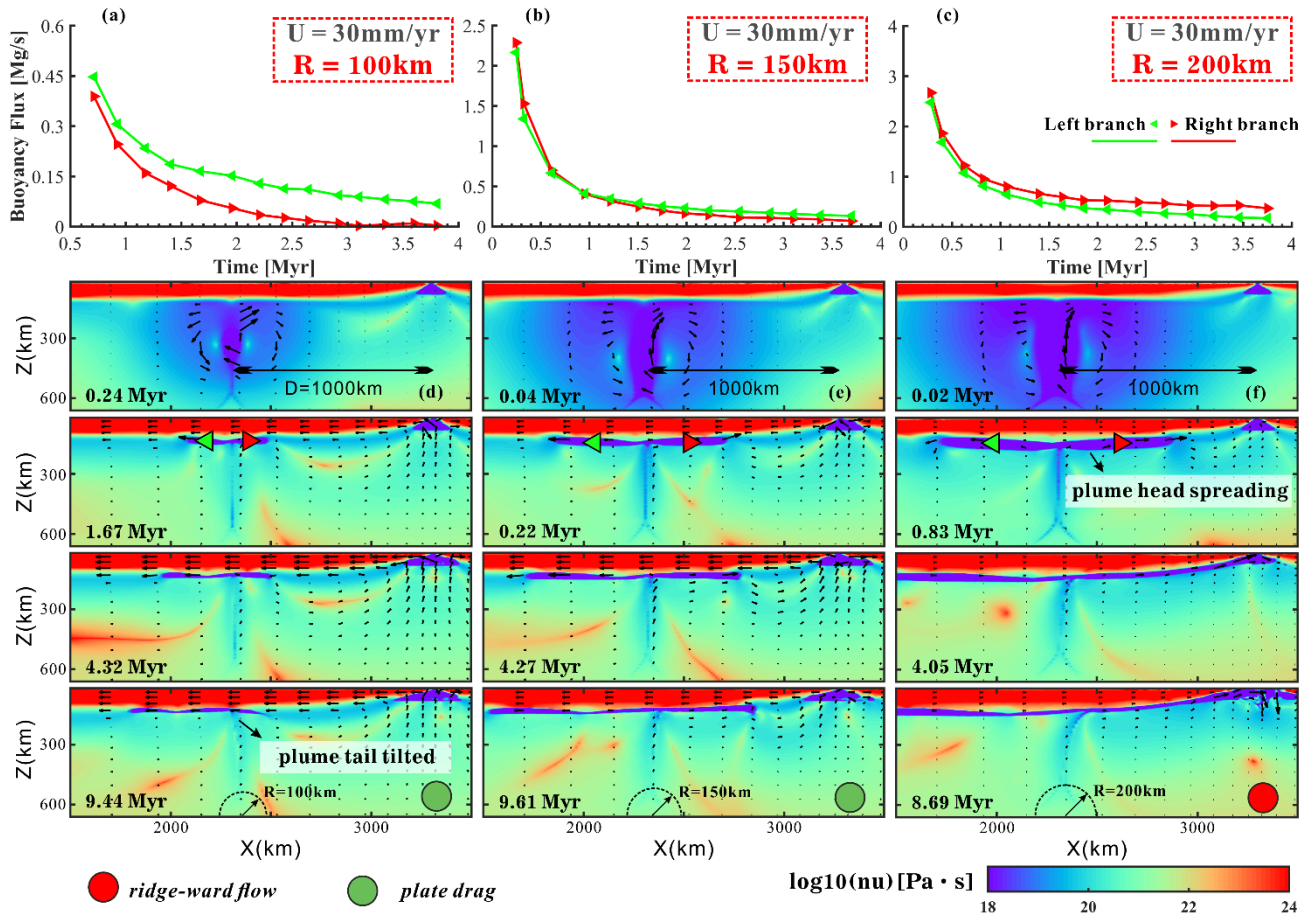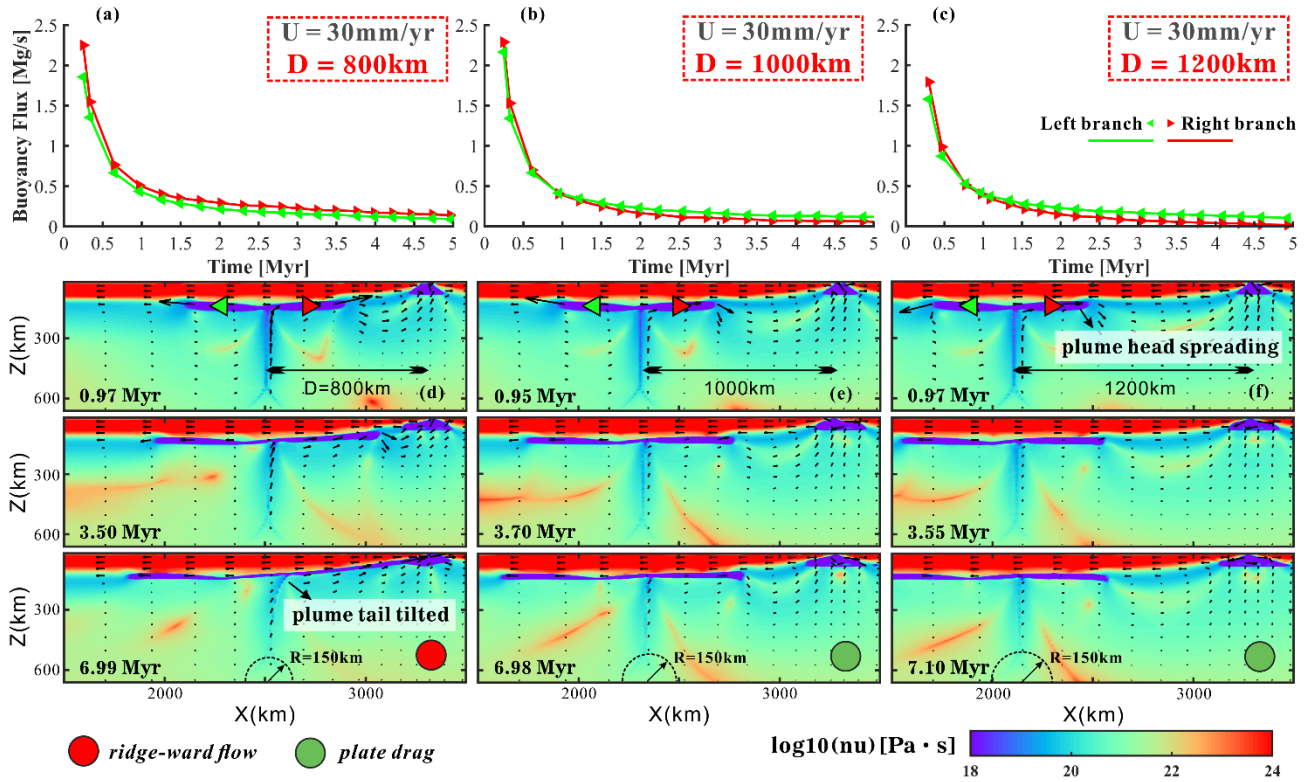
Figure 6 Models varying initial plume head radii (model M53, M58, and M63, Table S1 in supplementary material) shown by buoyancy flux and viscosity. **(a-c)** Buoyancy flux in spreading plume branches over time. Green and red triangles are markers used for buoyancy flux calculation. **(d-f)** Viscosity snapshots of models with different plume head radii. Models with green circle represent plate-drag plume flow and ridge-ward plume flow in red.

3.4.2 Plume-ridge distance

Plume-ridge distance also controls the regime of plume-ridge interaction. A plume at large distances spreads similarly as a plume at a small distance, but is less likely to get affected by ridge suction (Figs. 7e,f). The pressure gradient between the plume and ridge drives the ridge-ward plume flow. However, the larger the plume-ridge distance, the smaller the pressure gradient would be (Fig.

21

356 S8b), resulting in a lower buoyancy flux across the plume pipe (Figs. 7a-c). In the cases of distant

357 plumes, the spreading of the plume head is strongly affected by plate drag (Figs. 7b, c). On the other

358 hand, the difficulty in sustaining ridge-ward plume flow may also link to the heat transfer between the

359 cold plate and the hot plume rocks. With gradually cooling from upper plate by heat conduction and

360 diffusion, the viscosity of plume increases as it cools. Such increasing viscosity slows the plume down,

361 stopping the ridge-ward plume flow eventually (Figs. 7e, f). Hence, for cases with large plume-ridge

362 distances and hence travel times, the ponding plume head cools and is ultimately carried away by the

363 moving plate.

364

Figure 7. Models varying plume-ridge distances (model M57-M59, Table S1 in supplementary material) shown by buoyancy flux and viscosity. **(a-c)** Buoyancy flux in spreading plume branches over time. Green and red triangles are markers used for buoyancy flux calculation. **(d-f)** Viscosity snapshots of models with different plume-ridge distances. Models with green circle represent plate-drag plume flow and ridge-ward plume flow in red.

370

3.4.3 Half spreading rate of ridge

Another parameter that is worth investigating is the spreading rate of the ridge. The modeling results indicate that fast-spreading ridges promote plume flow away from the ridge due to the friction (Figs.8 and 9a). With increasing spreading rate, the effect of plate shearing on plume-lithosphere interaction increases, as quantified by the spreading fraction. The spreading fraction γ (Eq.(14)) is defined here as the ratio of ridge-ward vs. plate-drag plume volume fluxes. We integrated the ridge-ward plume volume flux (right branch), V_{rw}, and plate-drag plume volume flux (left branch), V_{tw}. V_p is the total plume volume flux in the model. Ridge-ward plume spreading is dominant for positive γ; plate-drag plume spreading is dominant for negative γ.

$$\gamma = (V_{rw} - V_{tw})/V_p \qquad (14)$$

In the early stage (~1 Myr), pressure-driven flow dominates in all models and spreading fractions are positive, mainly driven by the expansion of the overpressured plume heads along the pressure gradient. After a certain time, the spreading fractions decrease dramatically with the decay of the mantle plume activity, representing the transition from the ridge-ward to the plate-drag regime in some cases. The characteristic spreading fractions after 8 Myr model time as a function of our model parameters are shown in Fig. 8. This compilation of our results reveals that the dominance of ridge-ward flow decreases with increasing spreading rate and off-axis distance, but significantly increases with plume size. For models with fast-spreading ridges, the parameter range of plate-drag flow dominated models is expanded, indicating the critical role of plate drag in restricting ridge-ward flow and plume-ridge interaction.

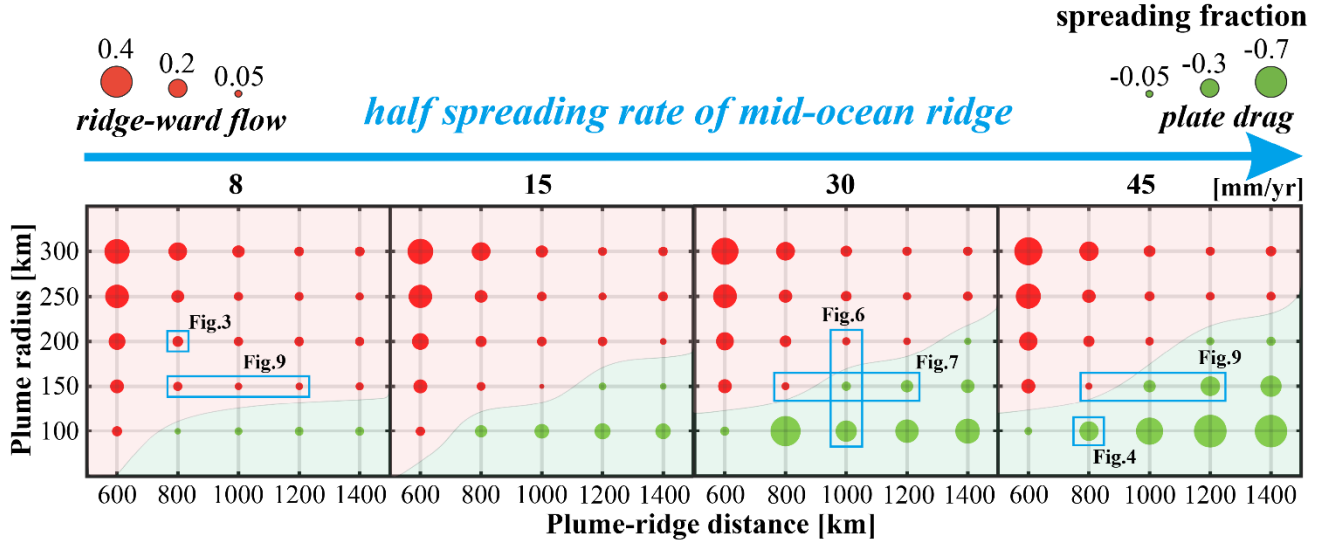**Figure 8.** Parameter regime diagram of the contrasting modes of plume-ridge interaction. Spreading

fractions γ (Eq. (14)) at ~8 Myr model time. Each of the circles represents one of the numerical

experiments, and sizes refer to γ. Circles in red and green represent models with dominant ridge-ward

plume flow and plate drag, respectively.

The transition from ridge-ward (positive γ) to plate-drag (negative γ) flow in some of our cases

is mainly determined by the competition between the effects of pressure-driven plume head spreading

and plate shearing. The overpressure in the plume head drives plume materials towards the lower

pressure spreading center, while the moving plate shears plume away. Hence, we quantify the shear

force of the overriding oceanic plate on the plume head using an integral approach:

$$F_s = \int \sigma_{xz} \, dA \quad (15)$$

Equation (15) is employed to calculate the shear force, where F_s is the total shear force the

spreading oceanic plate exerts on the uppermost part of the plume. σ_{xz} is the shear stress on each

mantle plume gird cell, A refers to the area of each grid cell. The pressure gradients, both gravitational

and dynamic pressure, are calculated by tracing the plume markers according to equations (12-13). As the plume material rises to the base of the lithosphere, the shear force exerted by the plate increases over time. We find that the integrated shear force between the spreading plate and the plume increases significantly as half spreading rate increases (Fig. 9c).

Conversely, ridge spreading rates control gravitational and pressure-driven plume driving forces (Fig. 9d). Increasing the spreading rate of the ridge implies a smaller dynamic pressure gradient, because the pressure gradient is related to the plate thickness difference at the ridge and plume, which is dependent on the spreading rate. A fast-spreading ridge also implies a smaller gravitational gradient, because it leaves a more shallowly-dipping lithospheric base. Thus, relatively strong plate shearing combined with relatively small pressure and gravitational gradients tend to advance plate-drag plume flow for high spreading rates.
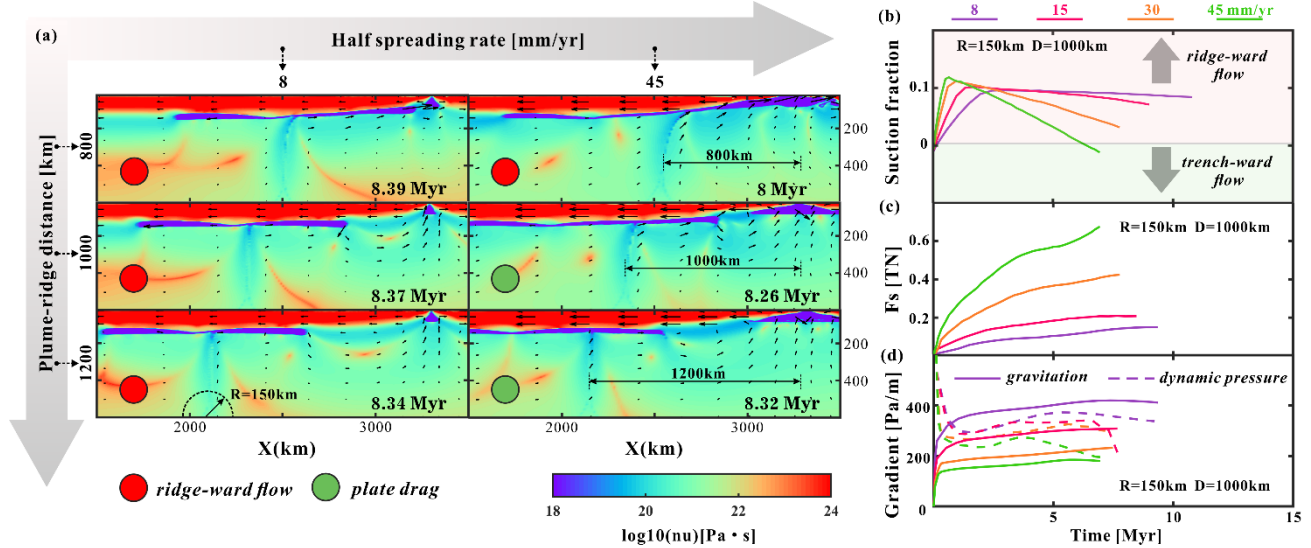
Figure 9. Model results influenced by different half spreading rates. **(a)** Effect of spreading rate on ridge-ward flow vs. plate-drag flow. Viscosity snapshots are shown (model M7-M9, M82-M84, Table S1 in supplementary material). Fast-spreading ridge promotes plume material dragged. Models with green circle represent plate-drag plume flow and ridge-ward plume flow in red. **(b)** Dynamic

25

423   evolutions of ridge-ward and plate-drag plume flow, revealed by defined ridge spreading fraction

424   (eq.14). **(c)** Shear force (*Fs*) between moving plate and plume material under different spreading rates.

425   **(d)** Pressure gradient between plume head and ridge center in different half spreading rate models. The

426   solid and dash lines are the plume gravitation and dynamic pressure gradient, respectively.

427

428

429   **4   Discussion**

430   Natural observations show that there are only very few hotspots indicative of ridge-ward plume

431   flow close to the East Pacific Rise (EPR) (Fig. 10a), in contrast to many such hotspots in the Atlantic

432   and Indian oceans. A previous study (Jellinek et al., 2003) proposed that fast-spreading ridges such as

433   the EPR efficiently convey any surrounding plumes into the spreading center from the deep mantle

434   (Fig. 1c), which leads to fewer hotspots nearby fast-spreading ridges. However, based on our modeling

435   results, fast-spreading ridges tend to promote plate-drag flow of the spreading plume material,

436   providing an alternative explanation to the relatively absence of hotspots along the EPR. We discuss

437   the viability of this potential explanation by comparing with geological and geophysical observations

438   (Fig. 10).

439   Firstly, the plate drag effect of fast-spreading ridges on plumes is evidenced by geophysical

440   observations. We locate the positions of the mantle plumes at the core-mantle boundary (CMB) and

441   the associated hot spots on the surface based on global seismic tomography (Jackson et al., 2021;

442   Koppers et al., 2021). A lateral offset between the deep and surface positions of plumes is a common

443   feature, indicating the deflection of plumes due to mantle flow. Specifically, a large portion of plumes

444   located in the Atlantic are tilted towards the mid-ocean ridge. However, only very few plumes in the

26

445 Pacific are tilted towards the mid-ocean ridge; indeed, the majority of plumes are tilted away from the

446 ridges, indicating the significant effect of plate drag on plumes beneath fast plates. Such observations

447 are consistent with the predictions of our models with dominant plate-drag plume spreading.

448
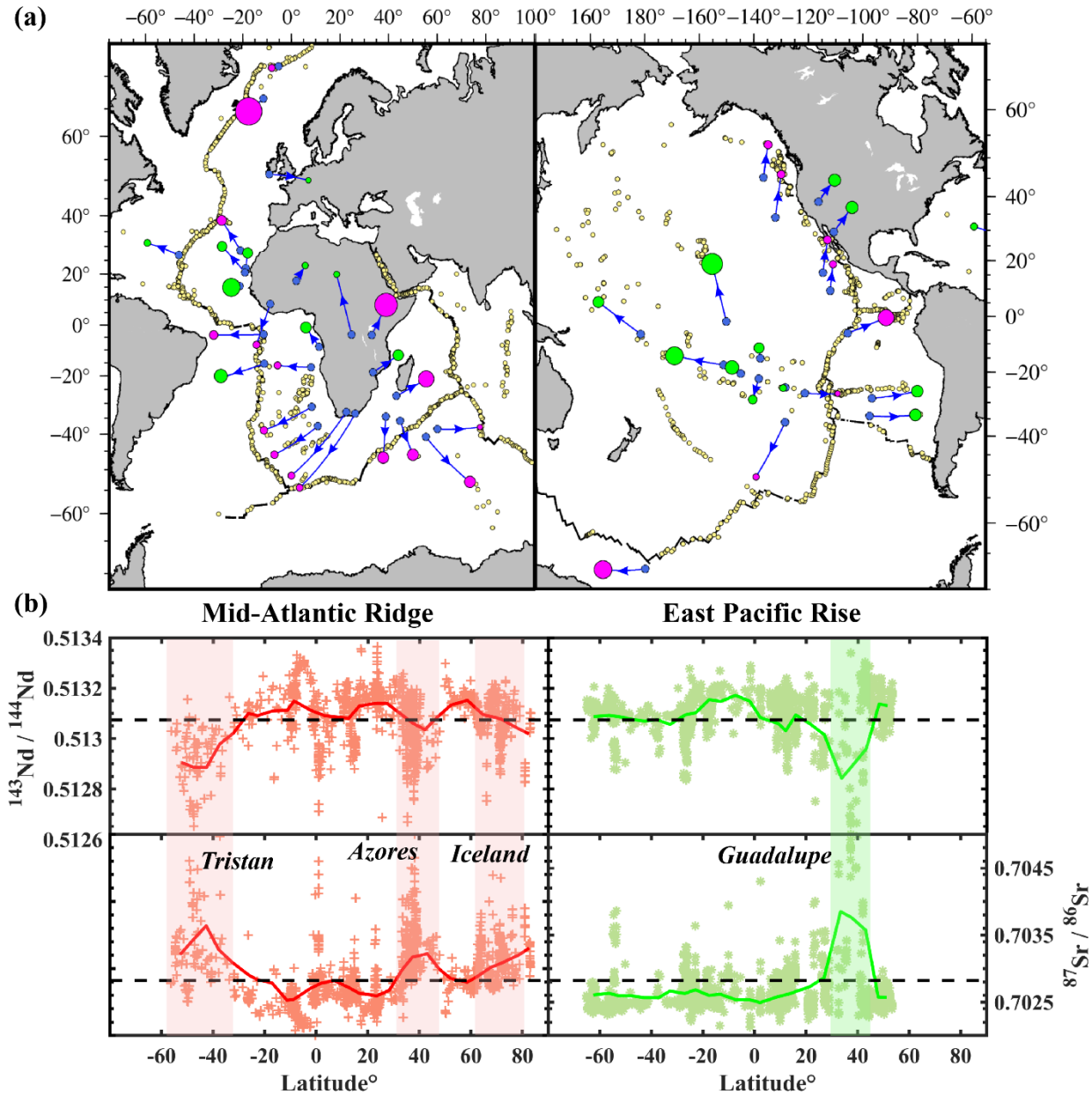
Figure 10. A compilation of hotspots along with spreading ridges in the Atlantic and the Pacific. **(a)**

Distribution of surface hotspots (circles) together with depth-projected source locations at CMB (blue

dots) of the plumes based on (Jackson et al., 2021). Plumes in magenta circles are mantle plumes

interacted with ridges (Ito et al., 2003), and plumes not interacted with ridges are shown as green

453 circles, whose size refers to the plume buoyancy flux (Hoggard et al., 2020). Yellow dots are MORB

454 samples mapped in (b). **(b)** Plot of radioactive isotopes ratios along ridge MORB samples. The data

455 are downloaded from the PetDB Database (http://portal.earthchem.org/). The colored symbols refer to

456 samples in different mid-ocean ridge. Main hotspots influencing MORBs are labeled with shaded

457 bands. The black dash lines are the mean MORB isotopes ratio from Gale (2013). Red and green lines

458 are the mean ratios of the samples in Mid-Atlantic ridge and EPR, respectively.

459

460   Geochemical studies suggest that mantle plumes are enriched in light rare earth elements (LREEs)

461 and radiogenic isotopes of Sr and Pb but depleted in Nd isotopes. These geochemical anomalies are

462 evident in MORB at the sites of active plume-ridge interaction (Cushman et al., 2004; Douglass and

463 Schilling, 1999; Yang et al. 2017). We find that MORB sampled along both the Mid-Atlantic ridge

464 and the EPR indeed display geochemical anomalies (Fig. 10b), indicating ridge-ward flow of plume

465 material at specific locations. However, the Mid-Atlantic MORB dataset is slightly more

466 heterogeneous than the East Pacific Rise in terms of geochemical isotopes. The EPR is basically

467 characterized as normal oceanic basalt, along which only very few regions show composition

468 associated with nearby plumes. This contradicts the view (Jellinek et al., 2003) that mantle plumes are

469 fully entrained into the central MOR melting zone at fast-spreading ridges.

470   Based on our modeling results, initial plume head radius and plume-ridge distance also control the

471 mode of plume-ridge interaction. However, there is only a small difference in terms of the fraction of

472 interacting vs. non-interacting plumes for different buoyancy fluxes B: a small majority of major

473 plumes (5 of 8 with $B > 1.6$ Mg/s) vs. a small minority of small-to-intermediate plumes (11 of 25 for

474 $B < 1.6$ Mg/s) display interaction with the ridge (Fig. 11a). The underlying cause for this observation

remains unclear, but may be related to the distribution of large plumes globally with many of them being located very far from MORs. Also note that our 2D models are limited in that plume material cannot spread in the out-of-plane direction, hence somewhat exaggerating the effects of buoyancy flux. In any case, the distribution of observed plume buoyancy fluxes (Hoggard et al., 2020) varies little across different oceans (Fig. 11a). Therefore, the effects of plume size are not a good candidate to explain the notable difference between the Atlantic and Pacific in terms of plume-ridge interaction mode.

On the other hand, compared with the Atlantic and Indian Oceans, Pacific plumes are located significantly further from the mid-ocean ridge (Fig. 11b). Plume-ridge distances in the Pacific are mostly >2000 km, which exceeds the maximum plume-ridge interaction distance of 1400 km (Schilling, 1991). Most plumes in the Pacific exhibit the typical signatures of plume flow away from the ridge, such as parabolic swell shapes (e.g., Society, Marquesas and Hawaii plumes; Ballmer et al., 2013a; Ballmer et al., 2015; Cheng et al., 2015; Wolfe et al., 2009), and linear volcanic chains (Buff et al., 2021; Clouard and Bonneville, 2005; Jackson et al., 2010). Age-progressive hotspots trails indicate an absence of dominant ridge-ward flow. By contrast, most plumes in the Atlantic have been close to the ridge since the opening of the ocean. These mantle plumes (e.g., Discovery, Iceland, Tristan-Gough; O'Connor et al., 2012) did not move much since the breakup of the Atlantic. One factor may be that the underlying plume generation zone (i.e., the edge of the African LLSVP) round largely parallel to the Mid-Atlantic Ridge (Fig. 1) (Torsvik et al., 2006). In this case, plume-ridge distance may play a critical role in the plume-ridge interaction, and could explain the striking difference between the Pacific and Atlantic in terms of the number of plume-ridge interacting vs. non-interacting systems. In addition, the rapid movement of the Pacific plate tends to inhibit ridge-ward plume flow at a given

497 plume-ridge distance. The distribution of interacting (stars) vs non-interacting systems in Figure 11b

498 is almost exactly as predicted by our models for the coupled effects of plume-ridge distance and plate

499 velocity. For example, we note that fast-spreading ridges can still interact with adjacent plumes under

500 the appropriate conditions. In the case of very short plume-ridge distances, there is good evidence of

501 plume-ridge interaction in the southern Pacific ocean (e.g., Louisville plume; Conder et al., 2002;

502 Toomey et al., 2002; Vlastélic and Dosso, 2005). Based on a series of numerical modeling as well as

503 geological and geophysical observations, we conclude that mantle plumes in the Pacific are more likely

504 to spread away from the ridge and into the direction of plate motion than in the Atlantic and Indian

505 Oceans. The tendency of fast plate velocities to promote plume spreading away from the MOR through

506 viscous drag may depend, however, on the details of lithosphere-asthenosphere rheological coupling

507 such as the presence of a weak decoupling (e.g., melt) layer (Rychert et al., 2020). Further studies of

508 plume spreading and plume-ridge interaction are needed to shed light on the coupling of the plate-

509 mantle system.
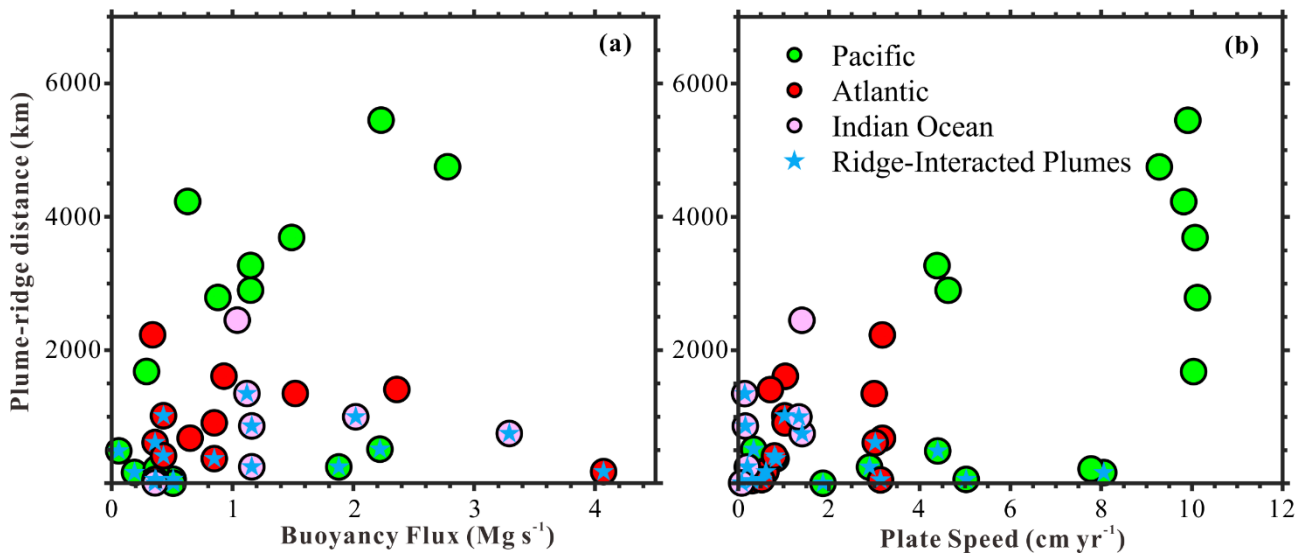
Figure 11. Buoyancy flux, plate speed and plume-ridge distance of mantle plumes in different oceans.

Mantle plumes in the Pacific, Atlantic and Indian Ocean are shown in green, red and pink circles,

respectively. Blue stars marked the ridge-interacted plumes according to Ito et al. (2003). **(a)** Plot of plume-ridge distance and plume buoyancy flux. Data are from Hoggard et al. (2020). **(b)** Plot of plume-ridge distance and plate speed at the location of plumes. Plume-ridge distance come from GPlates (Müller et al., 2016; Whittaker et al., 2015), and plate speed data come from Becker et al. (2015)

5   Conclusion

In this study, we explore the evolution of plume-ridge interaction with 2D thermomechanical numerical models. Based on model results, we find that:

(1) Plume-ridge interaction is mainly governed by the competition between the effects of plume spreading (overpressure in the plume-head stage), upward gravitationally-driven flow of the plume along the base of the sloping lithosphere and plate shearing. These driving forces are controlled by plume size, plume-ridge distance and the spreading rate of the mid-ocean ridge.

(2) MOR spreading does not only draw upwelling plumes into the spreading center, but also tends to drag mantle plumes away from the ridge. Plume flow away from the ridge is favored by small and/or distant plumes as well as slow spreading rates, whereas plume flow towards the ridge is promoted by large and/or nearby plumes, as well as slow spreading rates.

(3) Considering the high plate velocity and typically large plume-ridge distances, mantle plumes in the Pacific are more likely to be dragged away from the EPR than being drawn towards the ridge center.

Code availability

The source numerical modeling code in this study is available from the corresponding author upon reasonable request.

Data availability

The data that support the findings of this study are available from the corresponding author upon reasonable request.

Author contribution

Fengping Pang performed all numerical models, interpreted results and wrote the manuscript. Jie Liao proposed the study, modify the code and contributed to rewriting and scientific discussion. Maxim D. Ballmer contributed with significant help in rewriting and scientific discussion. Lun Li participated in discussion and interpretations. All authors have read and edited draft versions of the paper and have approved the final version.

Competing interest

The authors declare that they have no conflict of interest.

Acknowledgement

556 Numerical simulations were performed on the clusters of National Supercomputer Center in

557 Guangzhou (Tianhe-II).

558

Reference

Ballmer, M. D., Ito, G., Wolfe, C. J. and Solomon, S. C.: Double layering of a thermochemical plume in the upper mantle beneath Hawaii, Earth Planet. Sci. Lett., 376, 155–164, doi:10.1016/j.epsl.2013.06.022, 2013a.

Ballmer, M. D., Conrad, C. P., Smith, E. I. and Harmon, N.: Non-hotspot volcano chains produced by migration of shear-driven upwelling toward the East Pacific Rise, Geology, 41(4), 479–482, doi:10.1130/G33804.1, 2013b.

Ballmer, M. D., Ito, G. and Cheng, C.: Asymmetric dynamical behavior of thermochemical plumes and implications for hawaiian lava composition, Geophys. Monogr. Ser., 208, 35–57, doi:10.1002/9781118872079.ch3, 2015.

Barruol, G., Sigloch, K., Scholz, J. R., Mazzullo, A., Stutzmann, E., Montagner, J. P., Kiselev, S., Fontaine, F. R., Michon, L., Deplus, C. and Dyment, J.: Large-scale flow of Indian Ocean asthenosphere driven by Réunion plume, Nat. Geosci., 12(12), 1043–1049, doi:10.1038/s41561-019-0479-3, 2019.

Becker, T. W., Schaeffer, A. J., Lebedev, S. and Conrad, C. P.: Toward a generalized plate motion reference frame, Geophys. Res. Lett., 42(9), 3188–3196, doi:10.1002/2015GL063695, 2015.

Buff, L., Jackson, M. G., Konrad, K., Konter, J. G., Bizimis, M, Price, A., Rose-Koga, E. F., Blusztajn, J., Koppers, A. A. P. and Herrera, S.: "Missing Links" for the Long-lived Macdonald and Arago Hotspots, South Pacific Ocean, Geology, 49(5), 541–544, doi:10.1130/G48276.1, 2021.

Burov, E. and Cloetingh, S.: Erosion and rift dynamics: New thermomechanical aspects of post-rift evolution of extensional basins, Earth Planet. Sci. Lett., 150(1–2), 7–26, doi:10.1016/s0012-821x(97)00069-1, 1997.

Byerlee, J.: Friction of rocks, Pure Appl. Geophys. PAGEOPH, 116(4–5), 615–626, doi:10.1007/BF00876528, 1978.

Cheng, C., Allen, R. M., Porritt, R. W. and Ballmer, M. D.: Seismic constraints on a double-layered asymmetric whole-mantle plume beneath Hawai'i, Hawaiian Volcanoes From Source to Surf., 19–34, doi:10.1002/9781118872079.ch2, 2015.

Clouard, V. and Bonneville, A.: Ages of seamounts, islands, and plateaus on the Pacific plate, Spec. Pap. Geol. Soc. Am., 388, 71–90, doi:10.1130/0-8137-2388-4.71, 2005.

Conder, J. A., Forsyth, D. W. and Parmentier, E. M.: Asthenospheric flow and asymmetry of the East Pacific Rise, MELT area, J. Geophys. Res. Solid Earth, 107(B12), ETG 8-1-ETG 8-13, doi:10.1029/2001jb000807, 2002.

Cushman, B., Sinton, J., Ito, G. and Dixon, J. E.: Glass compositions, plume-ridge interaction, and hydrous melting along the Galapagos spreading center, 90.5 °wto 98 ° W, Geochemistry, Geophys. Geosystems, 5(8), doi:10.1029/2004GC000709, 2004.

Dalton, C. A., Langmuir, C. H. and Gale, A.: Geophysical and geochemical evidence for deep temperature variations beneath mid-ocean ridges, Science (80-.)., 344(6179), 80–83, doi:10.1126/science.1249466, 2014.

Douglass, J., Schilling, J. G. and Fontignie, D.: Plume-ridge interactions of the Discovery and Shona mantle plumes with the southern Mid-Atlantic Ridge (40°-55° S), J. Geophys. Res. Solid Earth, 104(B2), 2941–2962, doi:10.1029/98jb02642, 1999.

François, T., Koptev, A., Cloetingh, S., Burov, E. and Gerya, T.: Plume-lithosphere interactions in rifted margin tectonic settings: Inferences from thermo-mechanical modelling, Tectonophysics, 746(October 2015), 138–154, doi:10.1016/j.tecto.2017.11.027, 2018.

French, S. W. and Romanowicz, B.: Broad plumes rooted at the base of the Earth's mantle beneath major hotspots, Nature, 525(7567), 95–99, doi:10.1038/nature14876, 2015.

Gale, A., Dalton, C. A., Langmuir, C. H., Su, Y. and Schilling, J. G.: The mean composition of ocean ridge basalts, Geochemistry, Geophys. Geosystems, 14(3), 489–518, doi:10.1029/2012GC004334, 2013.

Geissler, W. H., Wintersteller, P., Maia, M., Strack, A., Kammann, J., Eagles, G., Jegen, M., Schloemer, A. and Jokat, W.: Seafloor evidence for pre-shield volcanism above the Tristan da Cunha mantle plume, Nat. Commun., (2020), doi:10.1038/s41467-020-18361-4, 2020.

Gerya, T.: Origin and models of oceanic transform faults, Tectonophysics, 522–523, 34–54, doi:10.1016/j.tecto.2011.07.006, 2012.

Gerya, T. V.: Three-dimensional thermomechanical modeling of oceanic spreading initiation and evolution, Phys. Earth Planet. Inter., 214, 35–52, doi:10.1016/j.pepi.2012.10.007, 2013.

Gerya, T. V. and Yuen, D. A.: Characteristics-based marker-in-cell method with conservative finite-differences schemes for modeling geological flows with strongly variable transport properties, Phys. Earth Planet. Inter., 140(4), 293–318, doi:10.1016/j.pepi.2003.09.006, 2003.

Gerya, T. V. and Yuen, D. A.: Robust characteristics method for modelling multiphase visco-elasto-plastic thermo-mechanical problems, Phys. Earth Planet. Inter., 163(1–4), 83–105, doi:10.1016/j.pepi.2007.04.015, 2007.

Gerya, T. V., Stern, R. J., Baes, M., Sobolev, S. V. and Whattam, S. A.: Plate tectonics on the Earth triggered by plume-induced subduction initiation, Nature, 527(7577), 221–225, doi:10.1038/nature15752, 2015.

Gülcher, A. J. P., Gerya, T. V., Montési, L. G. J. and Munch, J.: Corona structures driven by plume–

lithosphere interactions and evidence for ongoing plume activity on Venus, Nat. Geosci., 13(8), 547–554, doi:10.1038/s41561-020-0606-1, 2020.

Hardarson, B. S., Fitton, J. G., Ellam, R. M. and Pringle, M. S.: Rift relocation - A geochemical and geochronological investigation of a palaeo-rift in northwest Iceland, Earth Planet. Sci. Lett., 153(3–4), 181–196, doi:10.1016/s0012-821x(97)00145-3, 1997.

Harmon, N., Forsyth, D. W., Weeraratne, D. S., Yang, Y. and Webb, S. C.: Mantle heterogeneity and off axis volcanism on young Pacific lithosphere, Earth Planet. Sci. Lett., 311(3–4), 306–315, doi:10.1016/j.epsl.2011.09.038, 2011.

Hoggard, M. J., Parnell-turner, R. and White, N.: Hotspots and mantle plumes revisited: Towards reconciling the mantle heat transfer discrepancy, Earth Planet. Sci. Lett., 542, 116317, doi:10.1016/j.epsl.2020.116317, 2020.

Ito, G., Lin, J. and Gable, C. W.: Interaction of mantle plumes and migrating mid-ocean ridges: Implications for the Galfipagos plume-ridge system, , v, 1–3, 1997.

Ito, G., Lin, J. and Graham, D.: Observational and theoretical studies of the dynamics of mantle plume-mid-ocean ridge interaction, Rev. Geophys., 41(4), doi:10.1029/2002RG000117, 2003.

Jackson, M. G., Hart, S. R., Konter, J. G., Koppers, A. A. P., Staudigel, H., Kurz, M. D., Blusztajn, J. and Sinton, J. M.: Samoan hot spot track on a "hot spot highway": Implications for mantle plumes and a deep Samoan mantle source, Geochemistry, Geophys. Geosystems, 11(12), doi:10.1029/2010GC003232, 2010.

Jackson, M. G., Becker, T. W. and Steinberger, B.: Spatial Characteristics of Recycled and Primordial Reservoirs in the Deep Mantle, Geochemistry, Geophys. Geosystems, 22(3), doi:10.1029/2020GC009525, 2021.

647 Jellinek, A. M., Gonnermann, H. M. and Richards, M. A.: Plume capture by divergent plate motions:

648 Implications for the distribution of hotspots, geochemistry of mid-ocean ridge basalts, and estimates

649 of the heat flux at the core-mantle boundary, Earth Planet. Sci. Lett., 205(3–4), 361–378,

650 doi:10.1016/S0012-821X(02)01070-1, 2003.

651 Jiang, Q., Jourdan, F., Olierook, H. K. H., Merle, R. E. and Whittaker, J. M.: Longest continuously

652 erupting large igneous province driven by plume-ridge interaction, Geology, 1–3,

653 doi:10.1130/G47850.1, 2020.

654 Kincaid, C., Ito, G. and Gable, C.: Laboratory investigation of the interaction of off-axis mantle

655 plumes and spreading centres, Nature, 376(6543), 758–761, doi:10.1038/376758a0, 1995.

656 Kincaid, C., Schilling, J.-G. and Gable, C.: The dynamics of off-axis plume-ridge interaction in the

657 uppermost mantle, Earth Planet. Sci. Lett., 137(1–4), 29–43, doi:10.1016/0012-821X(95)00201-M,

658 1996.

659 Koppers, A. A. P., Becker, T. W., Jackson, M. G., Konrad, K., Müller, R. D., Romanowicz, B.,

660 Steinberger, B. and Whittaker, J. M.: Mantle plumes and their role in Earth processes, Nat. Rev.

661 Earth Environ., 2(6), 382–401, doi:10.1038/s43017-021-00168-6, 2021.

662 Lénat, J. F., Merle, O. and Lespagnol, L.: La réunion: An example of channeled hot spot plume, J.

663 Volcanol. Geotherm. Res., 184(1–2), 1–13, doi:10.1016/j.jvolgeores.2008.12.001, 2009.

664 Maia, M., Pessanha, I., Courrges, E., Patriat, M., Gente, P., Hémond, C., Janin, M., Johnson, K.,

665 Roest, W., Royer, J. Y. and Vatteville, J.: Building of the Amsterdam-Saint Paul plateau: A 10 Myr

666 history of a ridge-hot spot interaction and variations in the strength of the hot spot source, J.

667 Geophys. Res. Solid Earth, 116(9), 1–19, doi:10.1029/2010JB007768, 2011.

668 Mittelstaedt, E., Ito, G. and Behn, M. D.: Mid-ocean ridge jumps associated with hotspot

magmatism, Earth Planet. Sci. Lett., 266(3–4), 256–270, doi:10.1016/j.epsl.2007.10.055, 2008.

Mittelstaedt, E., Ito, G. and Van Hunen, J.: Repeat ridge jumps associated with plume-ridge

interaction, melt transport, and ridge migration, J. Geophys. Res. Solid Earth, 116(1), 1–20,

doi:10.1029/2010JB007504, 2011.

Mittelstaedt, E., Soule, S., Harpp, K., Fornari, D., McKee, C., Tivey, M., Geist, D., Kurz, M. D.,

Sinton, C. and Mello, C.: Multiple expressions of plume-ridge interaction in the Galápagos: Volcanic

lineaments and ridge jumps, Geochemistry, Geophys. Geosystems, 13(5),

doi:10.1029/2012GC004093, 2012.

Montelli, R., Nolet, G., Dahlen, F. A., Masters, G., Engdahl, E. R. and Hung, S. H.: Supporting

OnlineMaterial Timing, Science, 303(5656), 338–343, doi:10.1126/science.1092485, 2004.

Morgan, W. J.: Rodriguez, Darwin, Amsterdam, ..., A second type of Hotspot Island, J. Geophys.

Res. Solid Earth, 83(8), 5355–5360, 1978.

Müller, R. D., Roest, W. R. and Royer, J.-Y.: Asymmetric sea-floor spreading caused by ridge–

plume interactions, Nature, 396(6710), 455–459, doi:10.1038/24850, 1998.

Müller, R. D., Seton, M., Zahirovic, S., Williams, S. E., Matthews, K. J., Wright, N. M., Shephard,

G. E., Maloney, K. T., Barnett-Moore, N., Hosseinpour, M., Bower, D. J. and Cannon, J.: Ocean

Basin Evolution and Global-Scale Plate Reorganization Events since Pangea Breakup, Annu. Rev.

Earth Planet. Sci., 44, 107–138, doi:10.1146/annurev-earth-060115-012211, 2016.

Niu, Y.: Ridge suction drives plume-ridge interactions, , (October), doi:10.13140/2.1.4728.0961,

2014.

O'Connor, J. M., Jokat, W., Le Roex, A. P., Class, C., Wijbrans, J. R., Keßling, S., Kuiper, K. F. and

Nebel, O.: Hotspot trails in the South Atlantic controlled by plume and plate tectonic processes, Nat.

Geosci., 5(10), 735–738, doi:10.1038/ngeo1583, 2012.

Ranalli: Rheology of the Earth, 1995.

Ribe, N. M.: The dynamics of plume-ridge interaction: 2. Off-ridge plumes, , 101, 1996.

Ribe, N. M. and Christensen, U. R.: Three-dimensional modeling of plume-lithosphere interaction, , 99, 669–682, 1994.

Ribe, N. M. and Christensen, U. R.: The dynamical origin of Hawaiian volcanism, Earth Planet. Sci. Lett., 171(4), 517–531, doi:10.1016/S0012-821X(99)00179-X, 1999.

Ribe, N. M., Christensen, U. R. and Theißing, J.: The dynamics of plume-ridge interaction, 1: Ridge-centered plumes, Earth Planet. Sci. Lett., 134(1–2), 155–168, doi:10.1016/0012-821X(95)00116-T, 1995.

Rowley, D. B. and Forte, A. M.: Kinematics of the East Pacific Rise Retrodicted From Pacific and Farallon/Nazca Subduction-Related Torques: Support for Significant Deep Mantle Buoyancy Controlling EPR Spreading, J. Geophys. Res. Solid Earth, 127(2), 1–24, doi:10.1029/2020JB021638, 2022.

Rowley, D. B., Forte, A. M., Rowan, C. J., Glišović, P., Moucha, R., Grand, S. P. and Simmons, N. A.: Kinematics and dynamics of the east pacific rise linked to a stable, deep-mantle upwelling, Sci. Adv., 2(12), 1–19, doi:10.1126/sciadv.1601107, 2016.

Rychert, C. A., Harmon, N., Constable, S. and Wang, S.: The Nature of the Lithosphere-Asthenosphere Boundary, J. Geophys. Res. Solid Earth, 125(10), 1–39, doi:10.1029/2018JB016463, 2020.

Schilling, J. G.: Fluxes and excess temperatures of mantle plumes inferred from their interaction with migrating mid-ocean ridges, Nature, 352(6334), 397–403, doi:10.1038/352397a0, 1991.

713   Sleep, N. H.: Lateral flow and ponding of starting plume material, J. Geophys. Res. Solid Earth,

714   102(B5), 10001–10012, doi:10.1029/97jb00551, 1997.

715   Small, C.: Observations of ridge-hotspot interactions in the Southern Ocean, J. Geophys. Res.,

716   100(B9), doi:10.1029/95jb01377, 1995.

717   Straume, E. O., Gaina, C., Medvedev, S., Hochmuth, K., Gohl, K., Whittaker, J. M., Abdul Fattah,

718   R., Doornenbal, J. C. and Hopper, J. R.: GlobSed: Updated Total Sediment Thickness in the World's

719   Oceans, Geochemistry, Geophys. Geosystems, 20(4), 1756–1772, doi:10.1029/2018GC008115,

720   2019.

721   Toomey, D. R., Wilcock, W. S. D., Conder, J. A., Forsyth, D. W., Blundy, J. D., Parmentier, E. M.

722   and Hammond, W. C.: Asymmetric mantle dynamics in the MELT region of the East Pacific Rise,

723   Earth Planet. Sci. Lett., 200(3–4), 287–295, doi:10.1016/S0012-821X(02)00655-6, 2002.

724   Torsvik, T. H., Smethurst, M. A., Burke, K. and Steinberger, B.: Large igneous provinces generated

725   from the margins of the large low-velocity provinces in the deep mantle, Geophys. J. Int., 167(3),

726   1447–1460, doi:10.1111/j.1365-246X.2006.03158.x, 2006.

727   Turcotte, D. and Schubert, G.: Geodynamics, Cambridge University Press., 2014.

728   Vlastélic, I. and Dosso, L.: Initiation of a plume-ridge interaction in the South Pacific recorded by

729   high-precision Pb isotopes along Hollister Ridge, Geochemistry, Geophys. Geosystems, 6(5), 1–13,

730   doi:10.1029/2004GC000902, 2005.

731   Whittaker, J. M., Afonso, J. C., Masterton, S., Müller, R. D., Wessel, P., Williams, S. E. and Seton,

732   M.: Long-term interaction between mid-ocean ridges and mantle plumes, Nat. Geosci., 8(6),

733   doi:10.1038/NGEO2437, 2015.

734   Wolfe, C. J., Solomon, S. C., Laske, G., Collins, J. A., Detrick, R. S., Orcutt, J. A., Bercovici, D. and

735 Hauri, E. H.: Mantle shear-wave velocity structure beneath the Hawaiian hot spot, Science (80-.).,

736 326(5958), 1388–1390, doi:10.1126/science.1180165, 2009.

737 Yang, A. Y., Zhao, T. P., Zhou, M. F. and Deng, X. G.: Isotopically enriched N-MORB: A new

738 geochemical signature of off-axis plume-ridge interaction—A case study at 50°28′E, Southwest

739 Indian Ridge, J. Geophys. Res. Solid Earth, 122(1), 191–213, doi:10.1002/2016JB013284, 2017.

740
741